Atmospheric Environment 309 (2023) 119933

Contents lists available at ScienceDirect

Atmospheric Environment

journal homepage: www.elsevier.com/locate/atmosenv

A X_{CO_2} Retrieval Algorithm Coupled Spatial Correlation for the Aerosol and Carbon Detection Lidar

Zhipeng Pei [a,c], Ge Han [b,e,*], Tianqi Shi [a], Xin Ma [a], Wei Gong [a,d]

[a] State Key Laboratory of Information Engineering in Surveying, Mapping and Remote Sensing, Wuhan University, Wuhan, China
[b] School of Remote Sensing and Information Engineering, Wuhan University, Wuhan, China
[c] Hubei Luojia Laboratory, Wuhan, China
[d] Wuhan Institute of Quantum Technology, Wuhan, China
[e] Perception and Effectiveness Assessment for Carbon-neutral Efforts, Engineering Research Center of Ministry of Education, Wuhan, China

HIGHLIGHTS

- We propose a new algorithm for retrieving CO_2 for the first IPDA lidar satellite.
- The algorithm considering spatial correlation has a smaller random error.
- The results obtained by this algorithm can be verified using TCCON data.

GRAPHICAL ABSTRACT

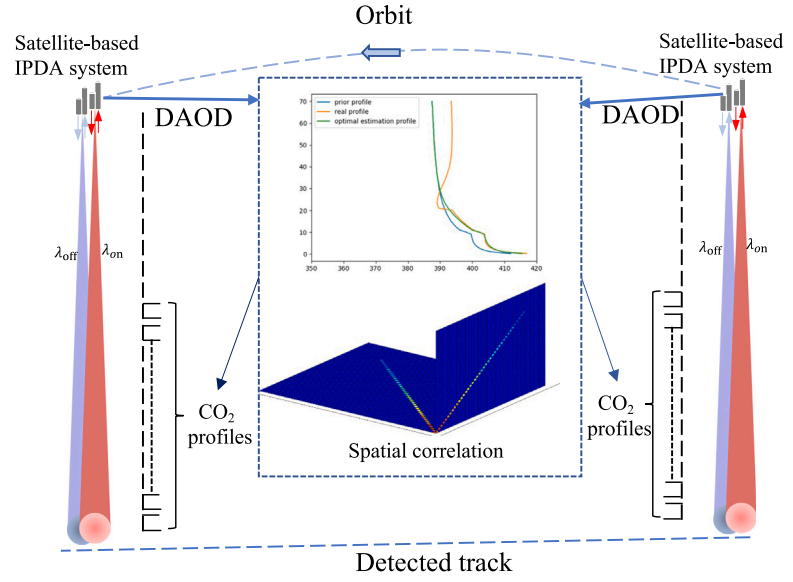

ARTICLE INFO

Keywords:
Carbon neutrality
IPDA
Atmospheric trace gases
Retrieval algorithms
Regularization

ABSTRACT

We describe the approach to estimating the atmospheric carbon dioxide (CO_2) for the Aerosol and Carbon Detection Lidar (ACDL) onboard the Atmospheric Environment Monitoring Satellite (AEMS). The method estimates the optimal state vector by maximizing the measurement posterior probability under a given prior state vector probability distribution. A priori constraint considering the spatial correlation is used as regularization to solve the ill-posed problem. We ran a series of observing system simulation experiments to demonstrate the critical outcome and character percentage uncertainty reduction. The results show that the state vector uncertainty can be reduced by ~ 10% near the surface for the single sounding. The CO_2 column-averaged dry air mole fraction (X_{CO_2}) derived by this algorithm is more stable than that obtained by the conventional algorithm and enables the monitoring of concentration changes for the multiple soundings.

* Corresponding author.
E-mail address: udhan@whu.edu.cn (G. Han).

https://doi.org/10.1016/j.atmosenv.2023.119933
Received 24 March 2023; Received in revised form 20 June 2023; Accepted 27 June 2023
Available online 1 July 2023

Similar to the Total Carbon Column Observing Network (TCCON), the averaging kernel is also provided for the subsequent flux inversion. Our simulation experiments demonstrate that the structure of the prior error covariance plays an important role in revealing vertical information from observations. In addition, we applied this algorithm to an airborne ACDL experiment for the retrieval of atmospheric CO_2 over Bohai Bay on March 14, 2019. AEMS's observations with a small footprint will yield important information on the carbon cycle, especially for small but strong emission sources.

1. Introduction

Greenhouse gases (GHGs), mainly carbon dioxide, are considered to be the most influential factor in global climate change, posing a serious challenge to global sustainable development (Eggleston et al., 2006; Pei et al., 2023). The international community has gradually reached a consensus that carbon emission reduction is the most effective way to curb global warming. The United Nations Framework Convention on Climate Change (UNFCCC) set out the need for measurable, reportable, and verifiable (MRV) national action to reduce emissions (Perugini et al., 2021). The 49th Intergovernmental Panel on Climate Change (IPCC) meeting recommended providing an independent, top-down assessment of emission inventories through atmospheric concentration observation (Buendia et al., 2019). The geographic distribution of stations in the ground-based observation networks (e.g., Network for the Detection of Atmospheric Composition Change (NDACC) and The Total Carbon Column Observing Network (TCCON)) is very heterogeneous, making it difficult to accurately understand the characteristics and mechanisms of source–sink changes of greenhouse gases. Satellite remote sensing has the advantages of objectivity, stability, and large coverage, and has become an indispensable technical tool for monitoring global atmospheric CO_2 concentrations. By detecting solar short-wave infrared radiation reflected from the surface, passive remote sensing satellites such as GOSAT, OCO-2 (O'Dell et al., 2012; Connor et al., 2008), and Tansat retrieve the CO_2 column-averaged dry air mole fraction (the ratio of the total number of CO_2 molecules to the total number of dry air molecules on the total column), called X_{CO_2}. Therefore, there are no effective observations at night or in high latitudes in winter. In addition, due to the interference of clouds and aerosols (Zhang et al., 2023), the data efficiency of passive remote sensing detection satellites is only about 10% (Dupuy et al., 2016), and the detection accuracy is also severely limited.

The Atmospheric Environment Monitoring Satellite (AEMS) (Li et al., 2022b; Meng et al., 2022; Han et al., 2018), also known as Daqi-1(DQ-1), was successfully launched on April 16, 2022. It operates in a sun-synchronous orbit, with a 705 km orbital altitude, a ~13:30 local overpass time, a 98.2° inclination, and a 16 days revisit rate. This platform is equipped with 5 instruments, including the Aerosol and Carbon Detection Lidar (ACDL) (Ke et al., 2022; Cao et al., 2022), the Particulate Observing Scanning Polarimeter (POSP) (Li et al., 2022a), the Directional Polarimetric Camera (DPC) (Li et al., 2018), the Environment Monitoring Instrument (EMI) (Zhang et al., 2020), and a wide field imaging spectrometer. ACDL, developed by the Shanghai Institute of Optics and Fine Mechanics, is the first spaceborne integrated-path differential absorption (IPDA) lidar system. As a prototype of the spaceborne IPDA lidar system, some airborne campaigns were conducted to test the instruments as well as the retrieval algorithms (Xiang et al., 2021). ACDL is expected to improve our understanding of the global distribution of carbon sources and sinks, especially at high latitudes, cloudy areas, and nighttime for supplementation. The conventional IPDA lidar algorithm takes the ratio of the measured CO_2 differential optical depth and the integrated weighting function (IWF) as the retrieval result (Refaat et al., 2016). However, note that this retrieval result cannot be directly verified using the TCCON due to the definition difference, which weights CO_2 concentration by IWF, rather than by the total number of dry air molecules. In this work, the definition of X_{CO_2} follows that of TCCON and is used to express the ratio of the number of CO_2 molecules to the total number of air molecules in the dry air column. To distinguish between the two, we use IWF-X_{CO_2} to denote the retrieval results obtained by the conventional lidar method. In addition, the IWF-X_{CO_2} of a single pulse is hard to be used directly due to measurement errors. Previous studies have often obtained the average IWF-X_{CO_2} by averaging over 30 s or longer.

Here, we develop a retrieval algorithm for AEMS based on the Bayesian optimal estimation (OE) and provide a general framework for similar atmospheric gas measurements. Unlike the least squares solution to the well-posed problem, Bayesian optimal estimation utilizes the informative prior covariance matrix to regularize the ill-posed problem, as described by Rodgers (2000). In addition to the constraints on the state vector by the diagonal elements of the prior covariance matrix (S_a), we configure non-diagonal elements considering the characteristics of a well-mixed GHG s concentration in practice. The S_a with such a structure can effectively avoid unphysical large wiggles in the posterior vertical profile and adjacent horizontal concentrations. And our definition of retrieved X_{CO_2} is consistent with that of the passive trace-gas column measurements (e.g., TCCON Wunch et al., 2011, OCO-2 Wunch et al., 2017, GOSAT Yokota et al., 2009, Tansat Yang et al., 2018, MethaneSAT Wofsy and Hamburg, 2019 and MethaneAIR Staebell et al., 2021). The paper is organized as follows. Section 2 describes the measurement principle of the IPDA lidar system and the instrument parameters. In Section 3, we introduce the retrieval algorithm proposed in this work in detail, as well as the error analysis involved in the subsequent experiments. In Section 4, we utilize observing system simulation experiments (OSSEs) to compare multiple retrieval strategies in different scenarios. In Section 5, this algorithm is applied to an airborne experiment of this IPDA lidar system. Section 6 describes the limitations and potential applications of the work. We then summarize the whole study in Section 7. This work is motivated by AEMS but is generally applicable to any column concentration retrieval of atmospheric trace gases.

2. Experimental setup

The schematic of IPDA lidar system is shown in Fig. 1. The main principle of IPDA lidar system is to measure the CO_2 differential absorption optical depth (DAOD) by using the difference in laser signal between the CO_2 central absorption line (on-line) and the absorption wing reference line (off-line) (Han et al., 2017a). The absorption cross-section of CO_2 molecules is large for on-line wavelengths and small for off-line wavelengths. Due to the small difference between on-line and off-line wavelengths, the interferences of aerosols and other gases are eliminated by the differential technique (Han et al., 2017a), which is one of the advantages of IPDA lidar system over the passive observation. Thus, it can be assumed that DAOD is caused only by CO_2 absorption in the column.

The main parameters of the airborne and spaceborne ACDL systems are listed in Table 1.

The photographs of the IPDA lidar system in the airborne experiment are shown in Fig. 2.

3. Method

Fig. 3 shows an overview of the retrieval algorithm for IPDA lidar system. Pre-processing includes processing of raw lidar data, calculation of optical range, estimation of signal-to-noise ratio (SNR), cloud

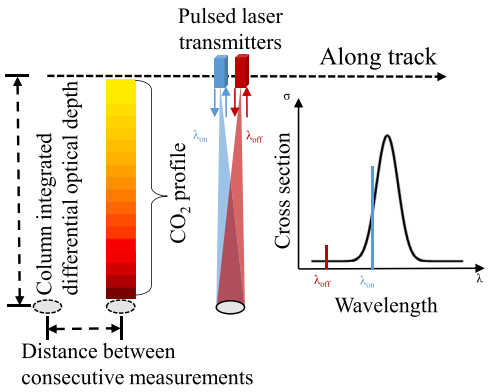

Fig. 1. Schematic of the 1.57-μm IPDA lidar measurements of the CO_2 DAOD.

Fig. 2. Photographs of the IPDA lidar system onboard Yun-8 aircraft.

Table 1
The main parameters of the airborne and spaceborne ACDL systems.

Parameters	Airborne value	Spaceborne value
Online wavelength	1572.024 nm	1572.024 nm
Offline wavelength	1572.085 nm	1572.085 nm
Pulse energy	6/3 (on/off) mJ	75 mJ
Pulse length (on/off)	17 ns	15 ns
Pulse separation	200 μs	200 μs
Repetition frequency	30 Hz	20 Hz
Pulse spectral linewidth (OPA)	30 MHz	50 MHz
Receiver optical efficiency	38%	52%
Telescope diameter	150 mm	1 m
Field of view	1 mrad	0.2 mrad
Dark current (noise equivalent power)	64 fw/$\sqrt{\text{Hz}}$	64 fw/$\sqrt{\text{Hz}}$
Optical filter bandwidth	0.45 nm	0.45 nm

identification, interpolation of meteorological data, and construction of prior state vectors. Spatial correlation matrix can be constructed based on location, reanalysis data, and practical considerations. Further the S_a matrix is constructed and fed into the forward model. The forward model and the retrieval strategy are described in detail in the next section.

3.1. Forward model

DAOD $\Delta\tau$ measured by IPDA lidar at a fixed altitude R_A is given by (Refaat et al., 2016)

$$\Delta\tau\left(\lambda_{on},\lambda_{off},R_A\right)=\ln\left\{\frac{P\left(\lambda_{off},R_A\right)\cdot t\left(\lambda_{off}\right)/E\left(\lambda_{off}\right)}{P\left(\lambda_{on},R_A\right)\cdot t\left(\lambda_{on}\right)/E\left(\lambda_{on}\right)}\right\}, \tag{1}$$

where P is received power (in watts) at wavelength λ, t is the effective pulse width of the return pulse at λ, and E is the transmitted laser energy at λ.

In addition, $\Delta\tau$ can be modeled integrally by Eq. (2) (Refaat et al., 2016)

$$\Delta\tau\left(\lambda_{on},\lambda_{off},R_A\right)=2\int_{R_A}^{0}\frac{\Delta\sigma\left(\lambda_{on},\lambda_{off},r\right)u(r)N_{dry}(r)}{10^6}\mathrm{d}r, \tag{2}$$

where $\Delta\sigma$ is the CO_2 differential cross section for the λ_{on} and λ_{off} wavelengths, $u(r)$ is CO_2 dry-air volume mixing ratio (VMR) in parts per million (ppm) at altitude r, and $N_{dry}(r)$ is the total molecular number density of dry air (in m^{-3}) at altitude r. The CO_2 absorption cross section varies with pressure and temperature. The simulated absorption cross sections at different altitudes is shown in Fig. 4, which are calculated by HAPI tool (Kochanov et al., 2016) and based on the HITRAN database (Rothman et al., 2009). The atmospheric column is usually divided into n layers from the surface to the observation position due to the nonlinear absorption cross section with respect to temperature and pressure. The interpolated cross sections at the center of each sub-layer are used to calculate the respective optical depths, which are then summed to obtain the total optical depth of atmospheric column. Similar to the Atmospheric CO_2 Observations from Space (ACOS) CO_2 retrieval algorithm (O'Dell et al., 2012), it is assumed that the CO_2 concentration at the center of the sublayer, varies linearly with pressure.

The forward model F described in Eq. (3) can relate the state vector x to the observation vector y,

$$y=F(x)+\epsilon, \tag{3}$$

where y is the measured DAOD provided by IPDA lidar system, x is CO_2 mixing ratio profile, and ϵ is assumed to be zero-mean, white Gaussian noise, which includes contributions from both the forward model error and the instrument error (Hou et al., 2016, 2020). Unlike passive remote sensing instruments, IPDA lidar systems rely on simple physical principles to derive the CO_2 abundance from the DAOD. The effects of aerosols and thin clouds are generally negligible (Han et al., 2017b). Therefore, we only considered the instrument error in this work for simplicity. For single soundings measurement, the dimensionality of the state vector is the number of air layers. For multiple soundings measurement, multiple profiles are retrieved simultaneously and the dimensionality of the state vector is the product of the number of soundings and the number of air layers.

3.2. Retrieval strategy

The solution to the retrieval problem is to find the statistically optimal x according to the given y. When sufficient observation information is available, the closed solution of the state vector can be obtained by the least squares method (Sun et al., 2021; Wunch et al., 2010), which is considered as a well-posed problem. When the observation information is not sufficient, the number of observed equations is smaller than the number of unknowns to be solved, which is considered as a ill-posed problem. In the optimal estimation algorithm as described in Rodgers (2000), the ill-posed problem can be solved by assuming a informative prior (Zeng et al., 2021; Zhou et al., 2019) or reducting dimensions (Ramanathan et al., 2018; Kulawik et al., 2017).

According to Bayes' theorem, the posterior probability density function (PDF) of the state vector x is given by

$$P(x\mid y)\propto P(y\mid x)P(x), \tag{4}$$

where $P(x)$ is the prior PDF of state vector and $P(y\mid x)$ is the conditional PDF of observation vector given the true state vector. Assuming $P(y\mid x)$ and $P(x)$ follow Gaussian distributions, posterior PDF can be given by

$$\begin{aligned}P(x\mid y)\propto exp\{&-\frac{1}{2}(x-x_a)^T S_a^{-1}(x-x_a)\\&-\frac{1}{2}(y-F(x))^T S_O^{-1}(y-F(x))\},\end{aligned} \tag{5}$$

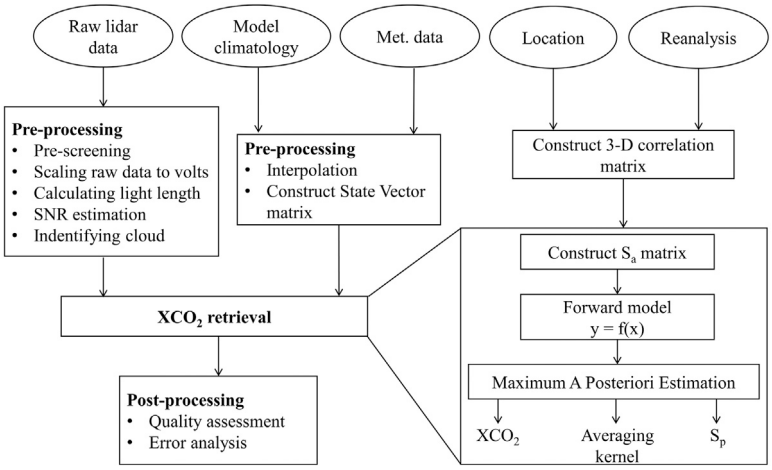

Fig. 3. Flowchart of the atmosphere CO_2 retrieval algorithm for the IPDA lidar system.

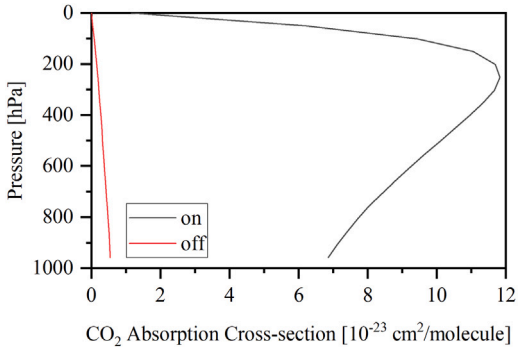

Fig. 4. Simulation of the CO_2 absorption cross section at λ_{on} and λ_{off} at different altitudes. The parameters of spectral lines are obtained from the HITRAN database and convolved with a Voigt profile. Values are for the US Standard Atmosphere (Anderson et al., 1986).

where x_a is the prior state vector, S_a is the error covariance matrix of the a priori state vector and S_O is the error covariance matrix of the observation vector. Eq. (6) gives the general solution for the maximum a posteriori (MAP) which is regarded as regularized a maximum likelihood estimate (MLE).

$$x_p = x_a + G\left(y - Kx_a\right) \tag{6}$$

where K is Jacobian of the state vector with respect to the measurement vector ($K = \frac{\partial y}{\partial x}$), also known as the weighting function matrix. G is the gain matrix, given by

$$G = \frac{\partial x}{\partial y} = \left(K^T S_O^{-1} K + S_a^{-1}\right)^{-1} K^T S_O^{-1} \tag{7}$$

The averaging kernel matrix A is given by

$$A = \frac{\partial x_p}{\partial x} = GK \tag{8}$$

A_{ij} describing the derivative of the retrieved state x_p at the ith level to the true state x at the jth level. The degree of freedom (DOF) of signal (Bowman et al., 2006) can be given by the trace of matrix A ($DOFs = tr(A)$). Substituting Eq. (3) into Eq. (6) and using Jacobian to expand $F(x)$, we obtain

$$x_p = x_a + A(x - x_a) + G\epsilon. \tag{9}$$

Intuitively, the retrieved x_p is not a straightforward estimate of the true state, but an estimate of a state smoothed by the averaging kernel. Nevertheless, the retrieval is sufficient to constraint the CO_2 flux for the further study. It is critical to simulate the x_p obtained by AEMS for a given CO_2 profile. The relationship between X_p and flux can be established by simulating true CO_2 profile in Eq. (9) with flux. The relationship between CO_2 profile and flux can be established by atmospheric transport model like Atmospheric Chemistry Model from Goddard Earth Observing System (GEOS-CHEM) for continental scale (Zhang et al., 2021; Shen et al., 2022), Community Multiscale Air Quality (CMAQ) model for national scale (Villalobos et al., 2020) and Stochastic Time-Inverted Lagrangian Transport Model (STILT) for megacity scale (Wu et al., 2018; Ye et al., 2020).

Ignoring the measurement error and multiplying both sides by pressure weighting function h^T in Eq. (9), we obtain

$$X^p_{CO_2} = X^a_{CO_2} + h^T A(x_m - x_a) \tag{10}$$

where n is the number of atmospheric layers, h is pressure weighting function and x_m is the simulated CO_2 profile. Details about h can be found in O'Dell et al. (2012). The adoption of averaging kernel matrix and prior state can remove the dependence of the x_p on the x_a and allows for the further flux-inversion studies.

3.3. Error analysis

The retrieval error is the difference between the retrieved x_p and the true state.

$$\delta x = x_p - x \tag{11}$$

Substituting Eq. (9) into Eq. (11) gives

$$\delta x = (I - A)(x - x_a) + G\epsilon. \tag{12}$$

where I is an identity matrix. Then we derive the total error or a posteriori covariance matrix from these two sources as

$$S_p = \underbrace{(I - A)S_a(I - A)^T}_{Smoothing\ \ Error} + \underbrace{GS_OG^T}_{Instrument\ \ Error} \tag{13}$$

Recasting,

$$S_p = \left(K^T S_O^{-1} K + S_a^{-1}\right)^{-1}. \tag{14}$$

S_p can be characterized with the uncertainties of the a priori state and the instrument noise (Kuai et al., 2016). The percentage uncertainty reduction is a good indicator to assess the potential of observations to constrain the CO_2 profile, which can be obtained (Villalobos et al., 2020), as follows:

$$U = (1 - \frac{\sigma_p}{\sigma_a}) \times 100\%, \tag{15}$$

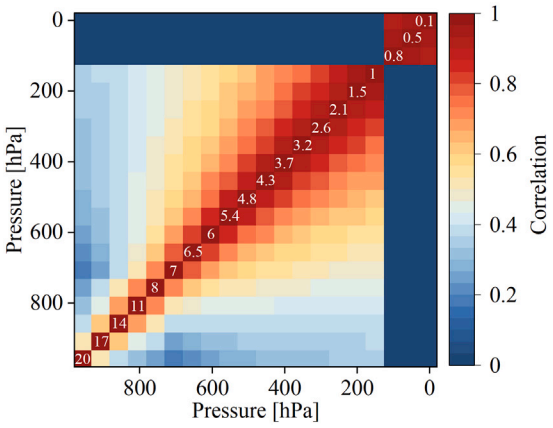

Fig. 5. A typical priori CO_2 error correlation matrix. The white numbers on the diagonal line represent the square root of diagonal elements of S_a. The colors indicate the error correlation between CO_2 concentrations at different layers, arranged TOA to surface from top to bottom and right to left.

where σ_a and σ_p are the square roots of the diagonal elements of S_a and S_p, respectively, that is the standard deviation of the prior and posterior. According to the definition of h ($X_{CO_2} = h^T x$), the error variance of retrieved $X^p_{CO_2}$ is give by

$$\sigma^2_{X^p_{CO_2}} = h^T S_p h. \tag{16}$$

3.4. A priori constraints

CO_2 is a well-mixed gas vertically and horizontally in the troposphere due to its long enough lifetime. Measurements of CO_2 VMR show variations of up to 30% near the surface, and these variations decrease rapidly with increasing height (Griffith et al., 2002). The record of CO_2 observations clearly shows that CO_2 spreads very evenly throughout the global atmosphere. The prior CO_2 profile can be obtained from model climatology, which is considered accurate unless influenced by upstream sources (sinks). For instance, CO_2 concentration in the planetary boundary layer varies by a few tens of ppm, or even several tens, depending on the vertical and horizontal distance of the observation point from the emission sources (e.g., the coal-fired power plant and densely populated industrialized city) (Yang et al., 2023). Following some previous studies (Baker et al., 2022; Kunik et al., 2019; Lauvaux et al., 2016), the error correlation is considered to decay exponentially with distance in the vertical direction. The special features are the decreasing correlation length with increasing height and the lack of correlation between the stratosphere and troposphere, which is due to the characteristics of the vertical motion of the atmosphere (O'Dell et al., 2012). In principle, the calculation of the correlation length requires a true concentration distribution. Thus, the correlation length is chosen mostly based on practical considerations. Here we set the vertical correlation length near the surface to 5 km. The 1σ priori error is set slightly larger in order to give adequate freedom to the retrieval to yield a posteriori profile that may deviate more from the prior profile. Details of how correlations are obtained in single sounding and multiple soundings are presented in Appendix A.

A typical correlation matrix and the diagonal elements of S_a are shown in Fig. 5. In the simulation experiments, each atmospheric layer is subdivided into 20 sublayers equally in pressure. The largest concentration uncertainty occur in the near-surface layer, because the flux-induced concentration enhancement has the largest effect on this layer. Moreover, this enhancement becomes progressively weaker with increasing altitude up to the top of the troposphere. Mathematically, this is described as a positive correlation between adjacent layers.

Table 2
Description of single sounding and multiple soundings.

	Single sounding	Multiple soundings
Number of layers	20	20
Number of columns	1	5
Dimension of x_a	20	100
Purpose	Vertical correlation	Horizontal correlation

3.5. WRF-STILT

To obtain a more realistic concentration for the "emission scenario" of OSSEs, we use the Weather Research and Forecasting-Stochastic Time Inverted Lagrangian Transport (WRF-STILT) model to simulate concentration enhancement caused by anthropogenic carbon emissions. STILT (Lin et al., 2003) is an atmospheric transport model based on Lagrangian random wander theory, which uses footprint weights to quantify the sensitivity of the concentration at the observation location to the upstream source (sink). The specific principle is that by releasing a large number of air particles at the observation location and simulating the backward trajectory of these particles, the quantitative footprint value is determined by the total number of particles below the surface layer height and the residence time of each particle (Wu et al., 2018). The WRF model (Skamarock et al., 2019) is used to provide high spatial and temporal resolution meteorological fields to the STILT model, mainly including 2-D wind speed, air pressure, relative humidity, air density, etc. for different simulated layer heights (Liu et al., 2023).

The model uses an 1×1 km^2 meteorological calculations and urban carbon fluxes from Emissions Database for Global Atmospheric Research (EDGAR). Hourly WRF fields contain 51 vertical levels with boundary conditions from 6 h $0.5° \times 0.5°$ NCEP final operational global analysis data. The main physical module setup for the WRF operation is similar to the previous study (Ye et al., 2020). For the STILT simulations, 1000 particles are released and transported backward for up to 7 days with a temporal resolution of 1 h. We simulated the concentration enhancement downwind of a typical city in the afternoon of December 29, 2014. The vertical distance of the city from the overpass is about 60 km.

4. OSSEs

In the OSSEs, we designed single sounding experiment and multiple soundings experiment to illustrate the contribution of vertical and horizontal correlation, respectively. Specifically, the number of layers, the number of columns and the dimension of x_a in these two sets of experiments are shown in Table 2.

4.1. Single sounding

Here we investigate the vertical correlation with a simulated the single pulse measurement in two different scenarios, affected (in the plume) and unaffected (out of the plume) by emissions. The plume is simulated by WRF-STILT model and the simulated CO_2 profile in the plume is shown in Fig. 6(b). The large enhancement (20 ppm) is mainly below the boundary layer height compared to the background concentration. Correspondingly, we assume the true CO_2 profiles (black lines in Fig. 6), temperature and pressure profiles for two scenarios. Further, pseudo-measurements are generated with 3% instrument noise using the forward model described in Section 3.1. We selected a set of pseudo-observations to demonstrate the smoothness imposed by the vertical correlation structure on the a posteriori profiles. The main results are shown in Figs. 6–8.

Fig. 6 indicates that retrievals that take into account vertical correlation perform better by comparing with the true profiles, whether out of the plume (Fig. 6(a)) or in the plume (Fig. 6(b)). The same diagonal elements are used in the S_a of both strategies, whereas the

non-diagonal element of S_a without considering vertical correlation is zero, which assumes that the errors between different layers are uncorrelated. As shown in Fig. 6(a), the posterior profile is closer to the true than the prior, as is the X_{CO_2}. The retrieval without considering the vertical correlation is inadequate for the adjustment of the prior profile, mainly focusing on the near-surface with large prior errors and large differential absorption cross section. The same phenomenon is also shown in Fig. 6(b). And in this case, although the posterior is better than the prior, it is not optimized enough for the enhancement of near-surface concentrations. Similarly, the technique of imposing smoothness by defining correlations between the elements of the profile was applied in some previous studies (O'Dell et al., 2012; Kuai et al., 2016; Bowman et al., 2006).

Fig. 7 demonstrates the column averaging kernels for 4 cases. They have similar vertical structures, with maximum values near the surface and decreasing then increasing with increasing height at the troposphere. The column averaging kernels with vertical correlation considered are significantly higher than that not considered. The DOF was 0.986, 0.932, 0.9989, 0.9956 for the four cases, respectively. In the same scenario, the DOF with vertical correlation considered is smaller than the one without. This is due to the fact that more priori information is provided when the measurement is unchanged.

Fig. 8 shows the uncertainty reduction for 4 cases. There is a significant improvement in the uncertainty reduction of the retrieval considering the vertical correlation. The retrievals that do not take into account vertical correlation reduce the uncertainty only near the surface. The retrievals that take into account vertical correlation reduce the uncertainty across the column except in the stratosphere.

Note that although in principle the OE algorithm has the ability to obtain an a posteriori profile, the concentration of a layer alone cannot be used directly because it is not an independent observation. In other words, when using the satellite retrieval results to constrain the flux, we must use $X^p_{CO_2}$ (or x_p) accompanied with a priori profile and averaging kernel matrix to provide an independent assessment.

Due to instrument noise, the retrieval results of single sounding sometimes bring the false optimization. This random error can be eliminated by the scheme of averaging $\Delta\tau$ or averaging signals before log (Zhu et al., 2020). Next section we introduce a error covariance structure with horizontal correlation to addresses this issue.

4.2. Multiple soundings

We assume a set of true CO_2 profiles as "no emission scenario". Further, we simulate the enhanced CO_2 profiles using WRF-STILT model as "emission scenario". The true profile is about 10 to 20 ppm higher than the true profile near the surface due to the flux influence. For presentation purposes, we have selected only the five adjacent soundings. The error covariance matrices (S_a; an 100 × 100 matrix) considering vertical correlation (a) and not considering vertical correlation (b) are shown in Fig. 9. The mathematical expressions are shown in Appendix B. The submatrix from the lower left to the upper right corner represents sounding 1 to 5, respectively. The diagonal elements of the lower left submatrix represent the ground to the top of the atmosphere from the bottom to the top, respectively. Based on the conclusions of the previous section, vertical correlation is all considered in this section. The horizontal error correlation is considered to decay exponentially with distance. Here we set the horizontal correlation length to 10 km. We assume that measurement correlations (off-diagonal values of S_O) are zero because the pulses are regarded independent of each other.

The retrieval results are shown in Figs. 10 and 11. For the "no emission scenario" (left column), retrievals that do not take into account the horizontal correlation are likely to misadjust, like (a) and (d). A posteriori profiles (green lines) are worse than a priori profiles (red lines) by comparing the true profiles (black lines). Oppositely, retrievals (blue lines) that take into account the horizontal correlation can avoid

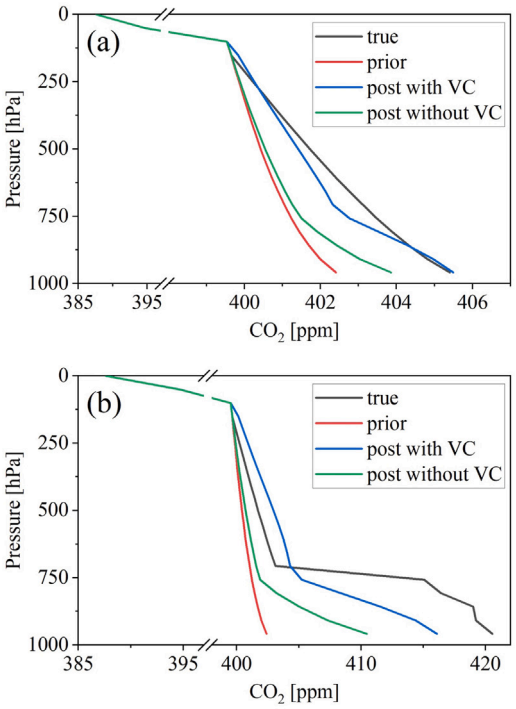

Fig. 6. Retrieved profiles for measurement of a simulated single pulse out of the plume (a) and in the plume (b). The black, red, blue, and green lines represent the true profiles, prior profiles, posterior profiles under vertical correlation (VC), and a posterior profiles without VC, respectively. The prior profiles in (a) and (b) are the same.

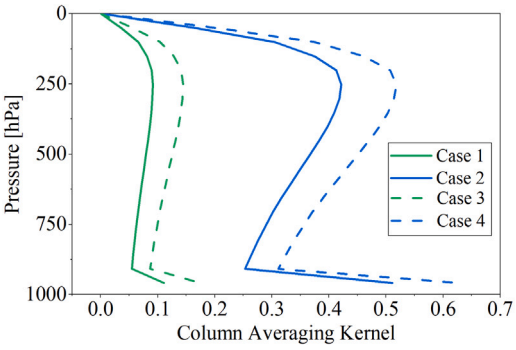

Fig. 7. Column averaging kernel for the single sounding. For case 1, not considering vertical correlation out of the plume. For case 2, considering vertical correlation out of the plume. For case 3, not considering vertical correlation in the plume. For case 4, considering vertical correlation in the plume.

this unexpected phenomenon. Fig. 11(a) also demonstrates the small variation of the posterior $X^p_{CO_2}$ considering the horizontal correlation.

For the "emission scenario" (right column), retrieved posterior profiles (blue lines) considering the horizontal correlation have better optimization. And most importantly, it can detect the changing gradient of the concentration at five locations, as also demonstrated by Fig. 11(b). The true X_{CO_2} was highest at the fourth sounding, which was less than 1 ppm higher than the others. The same trends can be seen in the posterior profiles (blue line) considering horizontal correlation. Although the true X_{CO_2} is always higher than the a posteriori $X^p_{CO_2}$, this does not affect the inversion of the fluxes. This is because this "bias" will be eliminated when extracting the concentration enhancement by subtracting the background concentration. In addition, it is normal for the true concentration enhancement to be larger than the a posteriori concentration enhancement due to the average kernel being less than

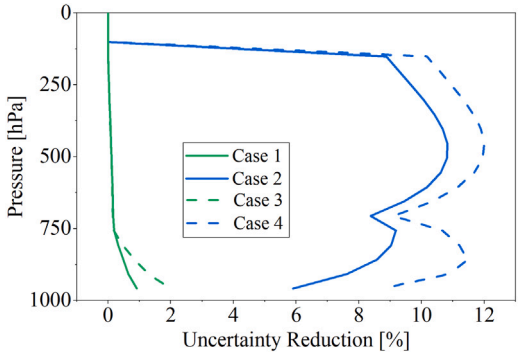

Fig. 8. The percentage uncertainty reduction. For case 1, not considering vertical correlation out of the plume. For case 2, considering vertical correlation out of the plume. For case 3, not considering vertical correlation in the plume. For case 4, considering vertical correlation in the plume.

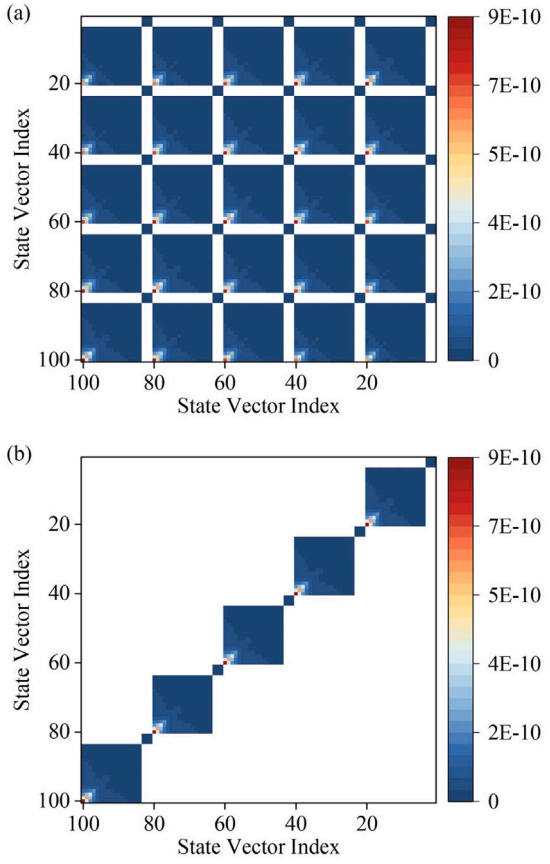

Fig. 9. The prior error covariance S_a structure considering horizontal correlation (HC) and not considering HC.

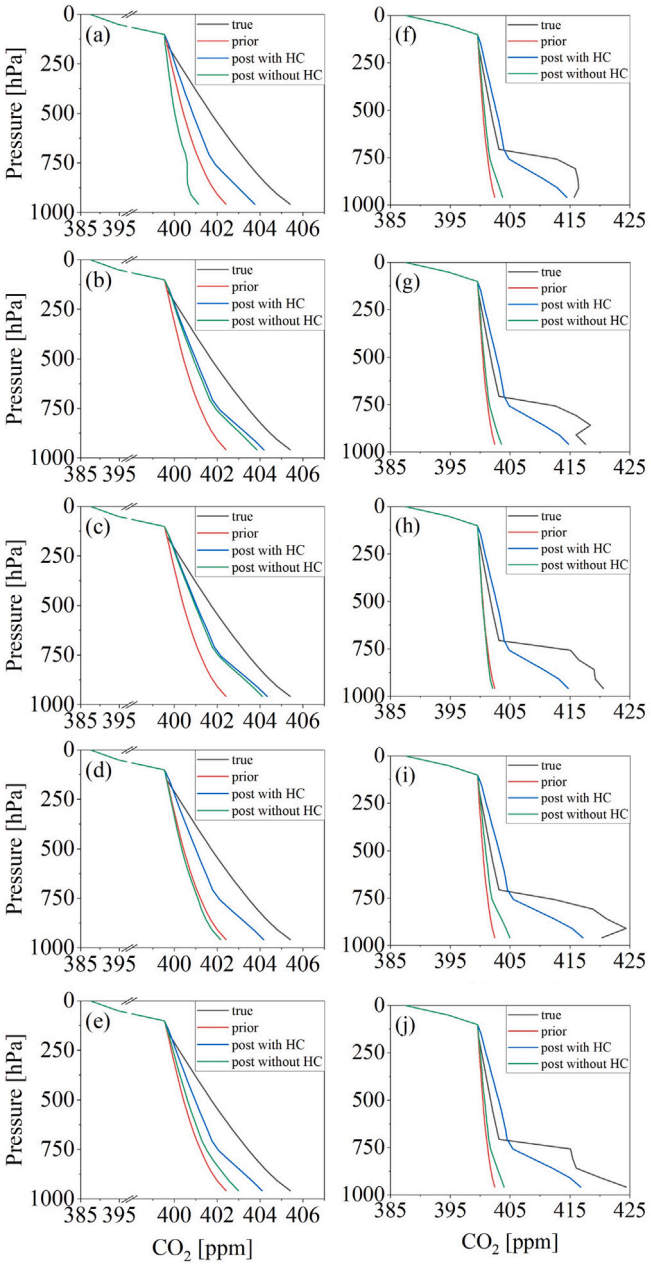

Fig. 10. Retrieved profiles for measurements of simulated multiple pulses. The left ((a)–(e)) and right ((j)–(i)) columns represent the "no-emissions scenario" and the "emissions scenario", respectively. The black, red, blue, and green lines represent the true, a priori, a posteriori under horizontal correlation (HC), and a posteriori without horizontal correlation profiles, respectively. The first to fifth rows represent each of the five soundings. The a priori profiles in the left and the right are the same.

1. It is worth mentioning that the extraction of relative changes in concentration is essential for the emission detection and flux inversion. A very small error in the posteriori X_{CO_2} can lead to a huge error in flux inversion.

In the "no emissions scenario", the DOF without considering the horizontal correlation and with considering the horizontal correlation are 4.937 and 4.931, respectively. In the "emissions scenario", the DOF without considering the horizontal correlation and with considering the horizontal correlation are 4.957 and 4.953, respectively.

Conventional retrieve method of IPDA lidar (Shi et al., 2021a; Han et al., 2017b) can only obtain IWF-X_{CO_2} (purple line in Fig. 11) without profile. Note that the definition of IWF-X_{CO_2} here is not the same as X_{CO_2} of TCCON (Wunch et al., 2011) due to the different weighting function. IWF-X_{CO_2} does not express the CO_2 column-averaged volume mixing ratio in the physical sense. Here we still compare the two X_{CO_2}s together in Fig. 11 in order to examine their relative changes. The IWF-X_{CO_2} fluctuations are very large due to instrument noise and the absence of a priori information constraints, regardless of the scenario. The averaging method is not suitable for measurements with a small number of available pulses. However, the OE algorithm that we adopt considering the horizontal correlation yields more stable and reliable results.

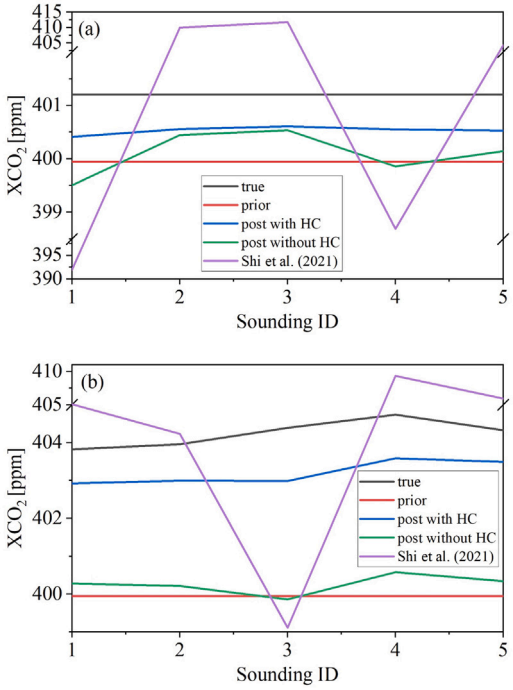

Fig. 11. Retrieved X_{CO_2} for measurements of simulated multiple pulses for the "no-emissions scenario" (a) and "emissions scenario" (b). The black, red, blue, green and purple lines represent of the true, a priori, a posteriori under horizontal correlation, a posteriori without horizontal correlation and IWF-derived X_{CO_2} (Shi et al., 2021a), respectively.

5. Airborne experiment

To elucidate the approach discribed in the previous sections, we apply this retrieval algorithm to an airborne validation experiment on March 14, 2019 over the Bohai Bay of China at 39.9° latitude and 119.6° longitude. This campaign is part of the AEMS. Main purpose of this campaign is evaluating the performance of the CO_2-IPDA lidar system produced by Shanghai Institute of Optics and Technology, which is carried on board of a YUN-8 aircraft. The aircraft took off from Shanhaiguan Airport, the flight altitude kept around 6.8 km, passing through ocean area (OA), residential area (RA) and mountainous area (MA), which covers multiple surface types of detection of AMES. In addition, an AIMMS-20 sensor was equipped to collect meteorological data, including temperature, humidity and pressure. GPS recorded latitude, longitude, and altitude information. And a greenhouse gas analyzer (LGR) recorded CO_2 concentrations at the flight altitude, which was notably that LGR was calibrated before the field campaign, using the standard concentration of CO_2 from 380 to 450 ppm. The data collected in range of 11:15:39 to 11:39:24 in local time was chosen for further analysis.

The detailed parameters of airborne CO_2-IPDA lidar system are shown in Table 1, on-line and off-line wavelength pulse would be formed through OPO laser unit with high stability. During the flight, the reflected signal from hard target through InGaAs photodiode (PD) detects to generate voltage signal, then, the light length (L_s) could be calculated by the speed of light and the propagation time of pulses. The difference between the GPS altitude and the ground altitude is used as the flight height (L_f) above ground level. The difference (d $= L_s - L_f$) between the light length and the flight height work as a judgment. When d is larger than 2000 m, it is considered as potential of the existence of clouds during the detected path, color CMOS camera equipped by YUN-8 aircraft could help us to determine the clouds' existence. Although we could retrieve the CO_2 concentration above and below clouds by the presented method of Shi et al. (2021a), it

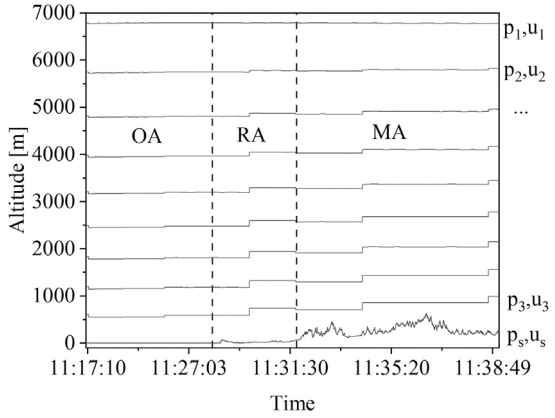

Fig. 12. The 10 pressure levels over three areas are given by p_i. u_i is a corresponding CO_2 VMR. The p_1 and p_s line represent the flight altitude and ground elevation.

was special cases in future measurements of AEMS. Therefore, the data for the presence of clouds are removed and not considered in this section. In addition, data with roll angle greater than 2 degrees were also excluded. The signals whose d is less than 50 m is selected to the validation experiment. DAOD was retrieved uses the integration method of the intensity of the pulse-echo signal, calculated by Eq. (1). Ideally, CO_2 distribution above ocean surface is stable, hence, the relative error (RE) of IPDA lidar system in this campaign is defined based on 600 pulses above ocean. See formula

$$RE = \frac{\sqrt{\frac{1}{N}\sum_{i=1}^{N}(DAOD_i - \overline{DAOD})}}{\overline{DAOD}}, \tag{17}$$

where $DAOD_i (i = 1, 2, 3...600)$ is the DAOD value calculated from the ith λ_{on} and λ_{off} pulse pairs $\overline{DAOD}$ is the average DAOD of selected 600 pulse pairs. We divide the atmosphere under the flight altitude into 10 layers with equal pressure, as shown in Fig. 12. The temperature, pressure and specific humidity at different altitudes are extracted from European Centre for Medium-Range Weather Forecasting (ECWMF) model forecast fields, which is used for ACOS CO_2 retrieval algorithm (O'Dell et al., 2012). The results of interpolation are shown in Fig. 13. The a priori CO_2 profile is provided by Carbon Tracker model, which is used for GFIT3 retrieval algorithm (Zeng et al., 2021). Similarly, vertical and horizontal correlations are applied in this section. The difference is that the airborne adjacent pulses have a shorter distance in space compared to the long distance between the footprint of the satellite. The error correlation is stronger for the concentrations of airborne-based adjacent detections. Thus, a larger horizontal correlation length was used in the retrieval of the airborne data. In addition, all soundings use the same a priori profile. And different soundings are considered to be uncorrelated with each other. We obtained the instrument noise by solving the standard deviation of a small piece of DAOD.

To reduce the computational cost of solving the inverse, we retrieve every 500 soundings as a group. A typical DOF for a group retrieval is 172.8. Fig. 14 demonstrates three typical retrievals over OA, RA and MA. Based on the structure of prior error covariance and observations, vertical information is revealed in principle. The profile over residential area is enhanced near surface due to human activities. In contrast, near-surface concentrations over OA and MA show a decrease compared to the a priori profile due to oceanic and ecological carbon sinks. And the reduction decreases with increasing height.

Figs. 15 and 16 shows the retrieved X_{CO_2} variations in spatial and temporal terms. First, it is quite intuitive to see that the residential area has significantly higher X_{CO_2} than the other two. This is consistent with the past knowledge that plants and oceans (Shi et al., 2021a) are considered as the main natural carbon sinks and cities as the main

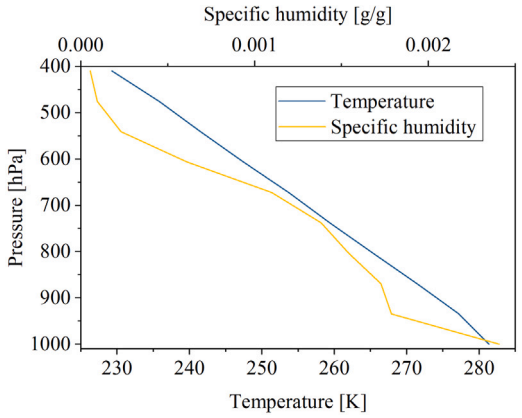

Fig. 13. The interpolated profiles of temperature, specific humidity from ECWMF dataset.

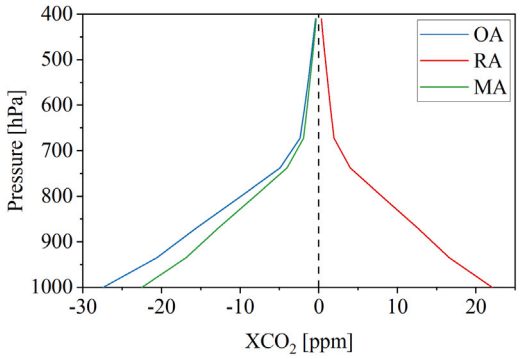

Fig. 14. The difference between posterior and the prior profile over ocean area (OA), residential area (RA) and mountainous area (MA).

anthropogenic carbon sources. In addition, Fig. 16 shows the trend of X_{CO_2} measured by the IPDA lidar system and the trend of the in-situ measurement instrument. It is worth noting that the X_{CO_2} measured by the IPDA lidar system is a column-averaged concentration, which is different from the concentration measured by the in-situ instrument at aircraft altitude. Therefore, it is not reasonable to directly compare these two measurements.

The large fluctuations of the initial DAOD will result in large fluctuations of IWF-X_{CO_2}. Zhu et al. (2020) and Xiang et al. (2021) adapted averaging approach to eliminate large fluctuations. Table 3 shows the comparison of the results between this work and Xiang et al.' work. Although the averaging approach is a fast and effective way to eliminate large fluctuations, this is based on the assumption that the concentrations are the same. When there is spatial variation in concentration, the averaging approach is hard to interpret. Therefore, based on the spatial correlation of the concentration, the preliminary results obtained by the OE algorithm coupled with spatial correlation not only have small standard deviation, but also represent well the gradients in the three regions. The mean value based on this work of the $X^p_{CO_2}$ over residential area is about 6 ppm higher than that over the other two regions. Due to the low reflectivity of the ocean surface, lidar obtains very weak echo signals in marine areas. The weak echo signal received over the ocean causes large standard deviation (σ) in the raw signal of DAOD and large fluctuations of $X^p_{CO_2}$. Using this relative change in concentration, the pressure weighting function and the averaging kernel matrix, it is sufficient to perform the top-down constraints on the carbon flux.

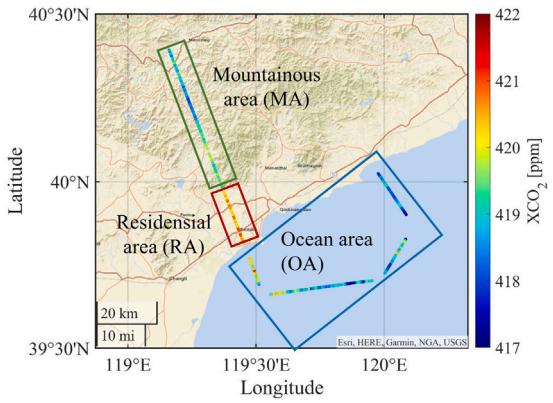

Fig. 15. Retrieved X_{CO_2} spatial variations. The blue, red, and green rectangular boxes represent ocean area (OA), residential area (RA), and mountainous area (MA), respectively.

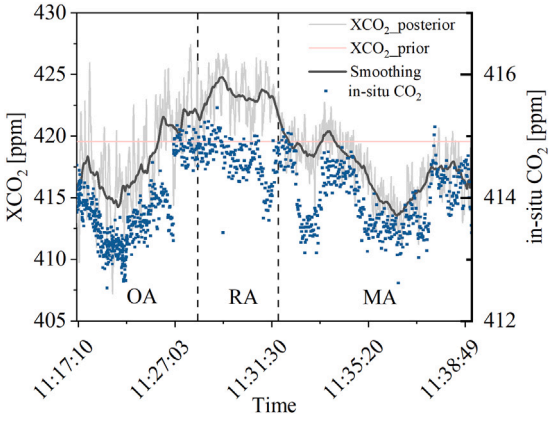

Fig. 16. Temporal variations of prior X_{CO_2}, posterior X_{CO_2} and in-situ CO_2 over ocean area (OA), residential area (RA), and mountainous area (MA). The posterior X_{CO_2} is smoothed with a 1000-point moving average for visual clarity.

Table 3
Comparison of retrieval results based on this work and conventional algorithm (Xiang et al., 2021). The Results of Xiang et al. are smoothed with a 600-point moving average.

Location	Mean		Standard deviation	
	This work	Xiang et al.	This work	Xiang et al.
Ocean area (OA)	417.88	411.05	3.7	9.76
Residential area (RA)	423.32	417.77	1.73	3.94
Mountainous area (MA)	417.32	410.72	2.42	3.88

6. Discussion

6.1. Bias in retrieved X_{CO_2}

All a priori configurations (e.g., atmospheric state and spectral parameters) may introduce errors into the retrieval. Consistent errors that cannot be reduced by averaging are categorized as "bias" errors. Wunch et al. (2017) pointed out that some biases due to systematic error can be removed by bias correction and residual biases that may be associated with surface properties but aerosol scattering still exist on a local scale, by comparison with TCCON's X_{CO_2} measurements. Fortunately, the fixed biases of X_{CO_2} will keep the concentration gradient unchanged and therefore will not affect the flux inversion (Ye et al., 2020).

Here we focus on the bias that the a priori CO_2 distribution may introduce into the results. Generally, we expect more independent information from the measurements by using as vague a priori information as possible. However, the informative prior is necessary for

the ill-posed problem without dimension reduction. Unlike the least squares approach, Bayes' law obtains the posterior not only from the measurement but also from the prior. The a priori bias-prone CO_2 profile may introduce unexpected bias into the a posteriori X_{CO_2}. The effect of these biases on X_{CO_2} enhancement could be eliminated with the subtraction of the biased background X_{CO_2} in a small spatial area(~200–300 km). Therefore, the determination of the background concentration plays an particularly important role in flux inversion. Observation-based methods (e.g., statistical or Lagrangian methods Pei et al., 2022) are suggested to generate the biased background X_{CO_2} to get the unbiased concentration enhancement.

6.2. Active–passive collaborative retrieval

The active IPDA lidar system has two distinct advantages. First, it is not affected by aerosols and thin clouds, and it can be eliminated by differential. Compared with the complex radiative transfer model of passive remote sensing, the forward model based on IPDA lidar system facilitates us to solve the state vector. Although the ACOS algorithm using full physics can give a rough estimate of AOD when the AOD is less than 0.3. Active IPDA lidar system can undoubtedly improve the data availability substantially. Second, passive remote sensing that relies on reflected sunlight cannot provide observations at night, and past space-based means cannot capture the day–night variation of CO_2 concentration, which is particularly important for carbon sink estimation (Kawa et al., 2010). In addition, DQ1-like satellites can also be used for inversion of fluxes (Wang et al., 2014) and estimation of point source emissions (Shi et al., 2021a). The error in X_{CO_2} is significantly correlated with the error in surface pressure. The typical surface pressure error of ECMWF is 2–3 hPa, which may be greater at high latitudes and high terrain areas. The advantage of passive remote sensing satellites (e.g., OCO-2) is that its Oxygen A-band is dedicated to the precise retrieval of surface pressure. Salstein et al. (2008). Furthermore, passive spectrometer offers the advantages of wide coverage and low cost. Daqi-2(DQ-2), equipped with an CO_2-IPDA lidar system and a passive spectrometer (Cai et al., 2022), is scheduled to be launched in 2025. Its products are expected to have the advantages of both passive and active remote sensing.

6.3. Multi-wavelength lidar measurements

The X_{CO_2} retrieval algorithm described in this study is used for the online and offline dual-wavelength IPDA lidar system. More wavelengths allow us to solve for more parameters (e.g., the Doppler shift and water vapor content) in addition to CO_2 and help to reduce bias in the X_{CO_2} retrieval. Although more wavelengths mean lower SNR due to the total average laser output power is fixed. The available wavelengths need to be chosen rationally based on the absorption lines of CO_2 and other interfering gases (Shi et al., 2023). For example, the laser should not be placed at a wavelength where the CO_2 absorption is so high that the received signal is too low for the retrieval (Shi et al., 2020). When the number of laser wavelengths is greater than the number of unknowns to be solved, least squares method (non-Bayesian) could be used without a priori information.

7. Conclusion

The retrieval algorithm proposed in this study for double-pulse IPDA lidar measurements is based on a Bayesian framework to estimate the X_{CO_2} by solving a constrained least squares problem. Regularization terms related to vertical and horizontal correlation are used to impose smoothing. OSSEs show that structure of prior error covariance play an important role in vertical distribution from the observations. The employment of vertical correlation is beneficial for the optimization of posterior profile and uncertainty reduction over the whole column.

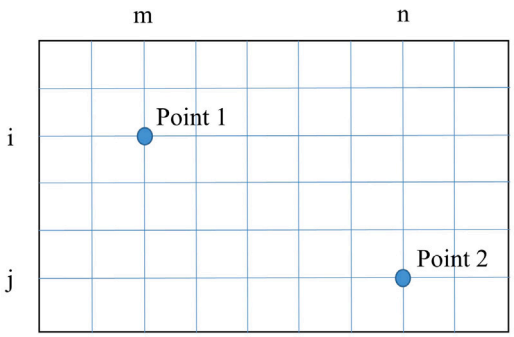

Fig. 17. Two points in a two-dimensional space. i and j denote layers i and j in the vertical direction. m and n denote columns m and n in the horizontal direction.

Horizontal correlation can be used to solve the problem of large posterior concentration fluctuations on the flight path, which is preferable especially when fewer effective detections are not enough to use the averaging method.

These techniques were applied to an airborne experiment, the pre-experiment of AEMS, near Bohai Bay, China, in March 2019. The echo signals were successfully received by the airborne-based IPDA lidar system. Compared with the conventional differential absorption ratioing approach, the a posteriori CO_2 column-averaged mixing ratio obtained in this study is able to detect concentration gradients without large fluctuations. Enhanced CO_2 concentrations of 6 ppm approximately are observed over the residential area.

Our future work will apply this retrieval algorithm to ACDL onboard AEMS and compare the retrievals with in situ measurements, such as TCCON or other passive remote sensing satellites.

CRediT authorship contribution statement

Zhipeng Pei: Conceptualization, Methodology, Writing – original draft. **Ge Han:** General guidance, Comments and discussion the results. **Tianqi Shi:** Methodology, Software. **Xin Ma:** General guidance. **Wei Gong:** General guidance.

Declaration of competing interest

The authors declare that they have no known competing financial interests or personal relationships that could have appeared to influence the work reported in this paper.

Data availability

Data will be made available on request.

Appendix A. Error correlation coefficient

As shown in Fig. 17, the error correlation coefficient between point 1 and point 2 can be calculated by Eq. (18),

$$\rho_{(1,2)} = \rho_{ij}^{\text{vertical}} \cdot \rho_{mn}^{\text{horizontal}} \tag{18}$$

where $\rho_{ij}^{\text{vertical}}$ the vertical correlation between the ith row and the jth row and $\rho_{mn}^{\text{horizontal}}$ the horizontal correlation between mth column and nth column. The horizontal and vertical correlation can be expressed based on exponential variogram:

$$\rho_{i,j} = \exp\left(-\frac{d_{i,j}}{L}\right) \tag{19}$$

where $d_{i,j}$ is the distance between point i and point j, and L is the correlation length.

Appendix B. The prior error covariance matrix

Here we give the prior error covariance matrix mathematically. Eqs. (20) and (21) correspond to (a) and (b) of Fig. 9, respectively.

$$\begin{bmatrix} P^{(1,5)} & P^{(2,5)} & P^{(3,5)} & P^{(4,5)} & S_a \\ P^{(1,4)} & P^{(2,4)} & P^{(3,4)} & S_a & P^{(5,4)} \\ P^{(1,3)} & P^{(2,3)} & S_a & P^{(4,3)} & P^{(5,3)} \\ P^{(1,2)} & S_a & P^{(3,2)} & P^{(4,2)} & P^{(5,2)} \\ S_a & P^{(2,1)} & P^{(3,1)} & P^{(4,1)} & P^{(5,1)} \end{bmatrix} \tag{20}$$

$$\begin{bmatrix} 0 & 0 & 0 & 0 & S_a \\ 0 & 0 & 0 & S_a & 0 \\ 0 & 0 & S_a & 0 & 0 \\ 0 & S_a & 0 & 0 & 0 \\ S_a & 0 & 0 & 0 & 0 \end{bmatrix} \tag{21}$$

where $S_a(20 \times 20)$ is the error covariance matrix of a single sounding, and $P^{(x,y)}(20 \times 20)$ is the error covariance matrix of the xth sounding and yth sounding. The ith row and jth column of $S_{a(i,j)}$ is $\sigma_i \cdot \rho_{ij}^{vertical} \cdot \sigma_j$. The ith row and jth column of $P_{(i,j)}^{(m,n)}$ is $\sigma_i \cdot \rho_{ij}^{vertical} \cdot \rho_{mn}^{horizontal} \cdot \sigma_j$, where $\rho_{ij}^{vertical}$ the vertical correlation efficient between xth and yth layers and $\rho_{mn}^{horizontal}$ is the horizontal correlation efficient between mth and nth soundings.

References

Anderson, G.P., Clough, S.A., Kneizys, F., Chetwynd, J.H., Shettle, E.P., 1986. AFGL Atmospheric Constituent Profiles (0.120 km). Technical Report, Air Force Geophysics Lab Hanscom AFB MA.

Baker, D.F., Bell, E., Davis, K.J., Campbell, J.F., Lin, B., Dobler, J., 2022. A new exponentially decaying error correlation model for assimilating OCO-2 column-average CO 2 data using a length scale computed from airborne lidar measurements. Geosci. Model Dev. 15 (2), 649–668.

Bowman, K.W., Rodgers, C.D., Kulawik, S.S., Worden, J., Sarkissian, E., Osterman, G., Steck, T., Lou, M., Eldering, A., Shephard, M., et al., 2006. Tropospheric emission spectrometer: Retrieval method and error analysis. IEEE Trans. Geosci. Remote Sens. 44 (5), 1297–1307.

Buendia, E., Tanabe, K., Kranjc, A., Baasansuren, J., Fukuda, M., Ngarize, S., Osako, A., Pyrozhenko, Y., Shermanau, P., Federici, S., 2019. Refinement to the 2006 IPCC Guidelines for National Greenhouse Gas Inventories, Vol. 5. IPCC, Geneva, Switzerland, p. 194.

Cai, M., Han, G., Ma, X., Pei, Z., Gong, W., 2022. Active–passive collaborative approach for XCO 2 retrieval using spaceborne sensors. Opt. Lett. 47 (16), 4211–4214.

Cao, X., Zhang, L., Zhang, X., Yang, S., Deng, Z., Zhang, X., Jiang, Y., 2022. Study on the impact of the Doppler shift for CO2 lidar remote sensing. Remote Sens. 14 (18), 4620.

Connor, B.J., Boesch, H., Toon, G., Sen, B., Miller, C., Crisp, D., 2008. Orbiting carbon observatory: Inverse method and prospective error analysis. J. Geophys. Res.: Atmos. 113 (D5).

Dupuy, E., Morino, I., Deutscher, N.M., Yoshida, Y., Uchino, O., Connor, B.J., De Mazière, M., Griffith, D.W., Hase, F., Heikkinen, P., et al., 2016. Comparison of XH2o retrieved from GOSAT short-wavelength infrared spectra with observations from the TCCON network. Remote Sens. 8 (5), 414.

Eggleston, H., Buendia, L., Miwa, K., Ngara, T., Tanabe, K., 2006. 2006 IPCC guidelines for national greenhouse gas inventories.

Griffith, D., Jamie, I., Leuning, R., Denmead, T., 2002. Surface fluxes of CO2, CH4, and N2O at OASIS'95 using tower-based FTIR techniques. Atmos. Environ. 36, 1833–1842.

Han, G., Cui, X., Liang, A., Ma, X., Zhang, T., Gong, W., 2017a. A CO 2 profile retrieving method based on chebyshev fitting for ground-based dial. IEEE Trans. Geosci. Remote Sens. 55 (11), 6099–6110.

Han, G., Ma, X., Liang, A., Zhang, T., Zhao, Y., Zhang, M., Gong, W., 2017b. Performance evaluation for China's planned CO2-IPDA. Remote Sens. 9 (8), 768.

Han, G., Xu, H., Gong, W., Liu, J., Du, J., Ma, X., Liang, A., 2018. Feasibility study on measuring atmospheric CO2 in urban areas using spaceborne CO2-IPDA LIDAR. Remote Sens. 10 (7), 985.

Hou, W., Wang, J., Xu, X., Reid, J.S., Han, D., 2016. An algorithm for hyperspectral remote sensing of aerosols: 1. development of theoretical framework. J. Quant. Spectrosc. Radiat. Transfer 178, 400–415.

Hou, W., Wang, J., Xu, X., Reid, J.S., Janz, S.J., Leitch, J.W., 2020. An algorithm for hyperspectral remote sensing of aerosols: 3. application to the GEO-TASO data in KORUS-AQ field campaign. J. Quant. Spectrosc. Radiat. Transfer 253, 107161.

Kawa, S., Mao, J., Abshire, J., Collatz, G., Sun, X., Weaver, C., 2010. Simulation studies for a space-based CO2 lidar mission. Tellus B 62 (5), 759–769.

Ke, J., Sun, Y., Dong, C., Zhang, X., Wang, Z., Lyu, L., Zhu, W., Ansmann, A., Su, L., Bu, L., et al., 2022. Development of China's first space-borne aerosol-cloud high-spectral-resolution lidar: retrieval algorithm and airborne demonstration. PhotoniX 3 (1), 17.

Kochanov, R.V., Gordon, I., Rothman, L., Wcisło, P., Hill, C., Wilzewski, J., 2016. HITRAN application programming interface (HAPI): A comprehensive approach to working with spectroscopic data. J. Quant. Spectrosc. Radiat. Transfer 177, 15–30.

Kuai, L., Worden, J.R., Li, K.-F., Hulley, G.C., Hopkins, F.M., Miller, C.E., Hook, S.J., Duren, R.M., Aubrey, A.D., 2016. Characterization of anthropogenic methane plumes with the hyperspectral thermal emission spectrometer (HyTES): A retrieval method and error analysis. Atmos. Meas. Tech. 9 (7), 3165–3173.

Kulawik, S.S., O'Dell, C., Payne, V.H., Kuai, L., Worden, H.M., Biraud, S.C., Sweeney, C., Stephens, B., Iraci, L.T., Yates, E.L., et al., 2017. Lower-tropospheric CO 2 from near-infrared ACOS-GOSAT observations. Atmos. Chem. Phys. 17 (8), 5407–5438.

Kunik, L., Mallia, D.V., Gurney, K.R., Mendoza, D.L., Oda, T., Lin, J.C., 2019. Bayesian inverse estimation of urban CO2 emissions: Results from a synthetic data simulation over salt lake city, UT. Elementa: Sci. Anthropocene 7.

Lauvaux, T., Miles, N.L., Deng, A., Richardson, S.J., Cambaliza, M.O., Davis, K.J., Gaudet, B., Gurney, K.R., Huang, J., O'Keefe, D., et al., 2016. High-resolution atmospheric inversion of urban CO2 emissions during the dormant season of the Indianapolis flux experiment (INFLUX). J. Geophys. Res.: Atmos. 121 (10), 5213–5236.

Li, Z., Hou, W., Hong, J., Fan, C., Wei, Y., Liu, Z., Lei, X., Qiao, Y., Hasekamp, O.P., Fu, G., et al., 2022a. The polarization crossfire (PCF) sensor suite focusing on satellite remote sensing of fine particulate matter PM2. 5 from space. J. Quant. Spectrosc. Radiat. Transfer 286, 108217.

Li, Z., Hou, W., Hong, J., Zheng, F., Luo, D., Wang, J., Gu, X., Qiao, Y., 2018. Directional polarimetric camera (DPC): Monitoring aerosol spectral optical properties over land from satellite observation. J. Quant. Spectrosc. Radiat. Transfer 218, 21–37.

Li, Z., Xie, Y., Hou, W., Liu, Z., Bai, Z., Hong, J., Ma, Y., Huang, H., Lei, X., Sun, X., et al., 2022b. In-orbit test of the polarized scanning atmospheric corrector (PSAC) onboard Chinese environmental protection and disaster monitoring satellite constellation HJ-2 A/B. IEEE Trans. Geosci. Remote Sens. 60, 1–17.

Lin, J., Gerbig, C., Wofsy, S., Andrews, A., Daube, B., Davis, K., Grainger, C., 2003. A near-field tool for simulating the upstream influence of atmospheric observations: The stochastic time-inverted Lagrangian transport (STILT) model. J. Geophys. Res.: Atmos. 108 (D16).

Liu, B., Ma, X., Guo, J., Li, H., Jin, S., Ma, Y., Gong, W., 2023. Estimating hub-height wind speed based on a machine learning algorithm: implications for wind energy assessment. Atmos. Chem. Phys. 23 (5), 3181–3193.

Meng, G., Wen, Y., Zhang, M., Gu, Y., Xiong, W., Wang, Z., Niu, S., 2022. The status and development proposal of carbon sources and sinks monitoring satellite system. Carbon Neutrality 1 (1), 32.

O'Dell, C., Connor, B., Bösch, H., O'Brien, D., Frankenberg, C., Castano, R., Christi, M., Eldering, D., Fisher, B., Gunson, M., et al., 2012. The ACOS CO 2 retrieval algorithm–part 1: Description and validation against synthetic observations. Atmos. Meas. Tech. 5 (1), 99–121.

Pei, Z., Han, G., Ma, X., Shi, T., Gong, W., 2022. A method for estimating the background column concentration of CO2 using the lagrangian approach. IEEE Trans. Geosci. Remote Sens. http://dx.doi.org/10.1109/TGRS.2022.3176134.

Pei, Z., Han, G., Mao, H., Chen, C., Shi, T., Yang, K., Ma, X., Gong, W., 2023. Improving quantification of methane point source emissions from imaging spectroscopy. Remote Sens. Environ. 295, 113652.

Perugini, L., Pellis, G., Grassi, G., Ciais, P., Dolman, H., House, J.I., Peters, G.P., Smith, P., Günther, D., Peylin, P., 2021. Emerging reporting and verification needs under the Paris agreement: How can the research community effectively contribute? Environ. Sci. Policy 122, 116–126.

Ramanathan, A.K., Nguyen, H.M., Sun, X., Mao, J., Abshire, J.B., Hobbs, J.M., Braverman, A.J., 2018. A singular value decomposition framework for retrievals with vertical distribution information from greenhouse gas column absorption spectroscopy measurements. Atmos. Meas. Tech. 11 (8), 4909–4928.

Refaat, T.F., Singh, U.N., Yu, J., Petros, M., Remus, R., Ismail, S., 2016. Double-pulse 2-μm integrated path differential absorption lidar airborne validation for atmospheric carbon dioxide measurement. Appl. Opt. 55 (15), 4232–4246.

Rodgers, C.D., 2000. Inverse Methods for Atmospheric Sounding: Theory and Practice, Vol. 2. World scientific.

Rothman, L.S., Gordon, I.E., Barbe, A., Benner, D.C., Bernath, P.F., Birk, M., Boudon, V., Brown, L.R., Campargue, A., Champion, J.-P., et al., 2009. The HITRAN 2008 molecular spectroscopic database. J. Quant. Spectrosc. Radiat. Transfer 110 (9–10), 533–572.

Salstein, D.A., Ponte, R.M., Cady-Pereira, K., 2008. Uncertainties in atmospheric surface pressure fields from global analyses. J. Geophys. Res.: Atmos. 113 (D14).

Shen, L., Gautam, R., Omara, M., Zavala-Araiza, D., Maasakkers, J., Scarpelli, T., Lorente, A., Lyon, D., Sheng, J., Varon, D., et al., 2022. Satellite quantification of oil and natural gas methane emissions in the US and Canada including contributions from individual basins. Atmos. Chem. Phys. Discuss. 1–22.

Shi, T., Han, G., Ma, X., Gong, W., Chen, W., Liu, J., Zhang, X., Pei, Z., Gou, H., Bu, L., 2021a. Quantifying CO2 uptakes over oceans using LIDAR: A tentative experiment in Bohai bay. Geophys. Res. Lett. 48 (9), e2020GL091160.

Shi, T., Han, G., Ma, X., Mao, H., Chen, C., Han, Z., Pei, Z., Zhang, H., Li, S., Gong, W., 2023. Quantifying factory-scale co2/ch4 emission based on mobile measurements and emission-partition model: cases in china. Environmental Research Letters 18 (3), 034028.

Shi, T., Han, G., Ma, X., Zhang, M., Pei, Z., Xu, H., Qiu, R., Zhang, H., Gong, W., 2020. An inversion method for estimating strong point carbon dioxide emissions using a differential absorption lidar. J. Clean. Prod. 271, 122434.

Skamarock, W.C., Klemp, J.B., Dudhia, J., Gill, D.O., Liu, Z., Berner, J., Wang, W., Powers, J.G., Duda, M.G., Barker, D.M., et al., 2019. A Description of the Advanced Research WRF Model Version 4, Vol. 145. National Center for Atmospheric Research, Boulder, CO, USA, p. 145.

Staebell, C., Sun, K., Samra, J., Franklin, J., Chan Miller, C., Liu, X., Conway, E., Chance, K., Milligan, S., Wofsy, S., 2021. Spectral calibration of the methaneair instrument. Atmos. Meas. Tech. 14 (5), 3737–3753.

Sun, X., Abshire, J.B., Ramanathan, A., Kawa, S.R., Mao, J., 2021. Retrieval algorithm for the column CO 2 mixing ratio from pulsed multi-wavelength lidar measurements. Atmos. Meas. Tech. 14 (5), 3909–3922.

Villalobos, Y., Rayner, P., Thomas, S., Silver, J., 2020. The potential of orbiting carbon observatory-2 data to reduce the uncertainties in CO 2 surface fluxes over Australia using a variational assimilation scheme. Atmos. Chem. Phys. 20 (14), 8473–8500.

Wang, J., Kawa, S., Eluszkiewicz, J., Baker, D., Mountain, M., Henderson, J., Nehrkorn, T., Zaccheo, T., 2014. A regional CO 2 observing system simulation experiment for the ascends satellite mission. Atmos. Chem. Phys. 14 (23), 12897–12914.

Wofsy, S.C., Hamburg, S., 2019. Methanesat-a new observing platform for high resolution measurements of methane and carbon dioxide. In: AGU Fall Meeting Abstracts, Vol. 2019. pp. A53F–02.

Wu, D., Lin, J.C., Fasoli, B., Oda, T., Ye, X., Lauvaux, T., Yang, E.G., Kort, E.A., 2018. A Lagrangian approach towards extracting signals of urban CO 2 emissions from satellite observations of atmospheric column CO 2 (XCO 2): X-stochastic time-inverted Lagrangian transport model ("x-STILT v1"). Geosci. Model Dev. 11 (12), 4843–4871.

Wunch, D., Toon, G.C., Blavier, J.-F.L., Washenfelder, R.A., Notholt, J., Connor, B.J., Griffith, D.W., Sherlock, V., Wennberg, P.O., 2011. The total carbon column observing network. Phil. Trans. R. Soc. A 369 (1943), 2087–2112.

Wunch, D., Toon, G.C., Wennberg, P.O., Wofsy, S.C., Stephens, B.B., Fischer, M.L., Uchino, O., Abshire, J.B., Bernath, P., Biraud, S.C., et al., 2010. Calibration of the total carbon column observing network using aircraft profile data. Atmos. Meas. Tech. 3 (5), 1351–1362.

Wunch, D., Wennberg, P.O., Osterman, G., Fisher, B., Naylor, B., Roehl, C.M., O'Dell, C., Mandrake, L., Viatte, C., Kiel, M., et al., 2017. Comparisons of the orbiting carbon observatory-2 (OCO-2) x CO 2 measurements with TCCON. Atmos. Meas. Tech. 10 (6), 2209–2238.

Xiang, C., Ma, X., Zhang, X., Han, G., Zhang, W., Chen, B., Liang, A., Gong, W., 2021. Design of inversion procedure for the airborne CO 2-IPDA LIDAR: A preliminary study. IEEE J. Sel. Top. Appl. Earth Obs. Remote Sens. 14, 11840–11852.

Yang, D., Liu, Y., Cai, Z., Chen, X., Yao, L., Lu, D., 2018. First global carbon dioxide maps produced from TanSat measurements.

Yang, S., Yang, J., Shi, S., Song, S., Luo, Y., Du, L., 2023. The rising impact of urbanization-caused CO2 emissions on terrestrial vegetation. Ecol. Indic. 148, 110079.

Ye, X., Lauvaux, T., Kort, E.A., Oda, T., Feng, S., Lin, J.C., Yang, E.G., Wu, D., 2020. Constraining fossil fuel CO2 emissions from urban area using OCO-2 observations of total column CO2. J. Geophys. Res.: Atmos. 125 (8), e2019JD030528.

Yokota, T., Yoshida, Y., Eguchi, N., Ota, Y., Tanaka, T., Watanabe, H., Maksyutov, S., 2009. Global concentrations of CO2 and CH4 retrieved from GOSAT: First preliminary results. Sola 5, 160–163.

Zeng, Z.-C., Natraj, V., Xu, F., Chen, S., Gong, F.-Y., Pongetti, T.J., Sung, K., Toon, G., Sander, S.P., Yung, Y.L., 2021. GFIT3: a full physics retrieval algorithm for remote sensing of greenhouse gases in the presence of aerosols. Atmos. Meas. Tech. 14 (10), 6483–6507.

Zhang, Y., Jacob, D.J., Lu, X., Maasakkers, J.D., Scarpelli, T.R., Sheng, J.-X., Shen, L., Qu, Z., Sulprizio, M.P., Chang, J., et al., 2021. Attribution of the accelerating increase in atmospheric methane during 2010–2018 by inverse analysis of GOSAT observations. Atmos. Chem. Phys. 21 (5), 3643–3666.

Zhang, Y., Wang, W., He, J., Jin, Z., Wang, N., 2023. Spatially continuous mapping of hourly ground ozone levels assisted by Himawari-8 short wave radiation products. GISci. Remote Sens. 60 (1), 2174280.

Zhang, X., Wang, F., Wang, W., Huang, F., Chen, B., Gao, L., Wang, S., Yan, H., Ye, H., Si, F., et al., 2020. The development and application of satellite remote sensing for atmospheric compositions in China. Atmos. Res. 245, 105056.

Zhou, M., Langerock, B., Sha, M.K., Kumps, N., Hermans, C., Petri, C., Warneke, T., Chen, H., Metzger, J.-M., Kivi, R., et al., 2019. Retrieval of atmospheric CH 4 vertical information from ground-based FTS near-infrared spectra. Atmos. Meas. Tech. 12 (11), 6125–6141.

Zhu, Y., Yang, J., Chen, X., Zhu, X., Zhang, J., Li, S., Sun, Y., Hou, X., Bi, D., Bu, L., et al., 2020. Airborne validation experiment of 1.57-μm double-pulse IPDA LIDAR for atmospheric carbon dioxide measurement. Remote Sens. 12 (12), 1999.